

The Standing Accretion Shock Instability in the Disk around the Kerr Black Hole

Hiroki Nagakura¹ and Shoichi Yamada^{1,2}

hiroki@heap.phys.waseda.ac.jp

ABSTRACT

This paper is a sequel to our previous work for accretion onto a Schwarzschild black hole and the so-called standing accretion shock instability (SASI), in this paper we investigate non-axisymmetric perturbations for a Kerr black hole. The linear and non-linear phases for the shock evolution are analyzed in detail by both 2D general relativistic hydrodynamical simulations and linear analysis. Since the structure of steady axisymmetric accretion flows with a standing shock wave is very sensitive to the inner transonic flow, their properties such as Mach numbers, which are important for the stability, depend on the Kerr parameter very much. Although the essential features of the instability do not differ from the previous results for the Schwarzschild black hole, the frame dragging effects specific to the Kerr black hole is also evident. Interestingly, the oscillation periods of the fundamental unstable modes are dependent only on the shock radius irrespective of the injection parameters.

Subject headings: black hole physics, hydrodynamics, instabilities, relativity, shock waves

1. Introduction

It is widely believed that the transonic rotating accretion flow onto a black hole is one of the candidate sources for many high energy astrophysical phenomena. The time variability of these objects may be interpreted as the unsteadiness of accretion flows, which in general suffer from various types of instabilities, such as thermal, viscous, dynamical, self-gravity, induced ones and so on. A variety of physical mechanisms (Varnie & Tagger (2002,

¹Science and Engineering, Waseda University, 3-4-1 Okubo, Shinjuku, Tokyo 169-8555, Japan

²Advanced Research Institute for Science and Engineering, Waseda University, 3-4-1 Okubo, Shinjuku, Tokyo 169-8555, Japan

2006); Dong & David (2008), and references therein) have been considered to explain the observed intensity variations. The shock wave in the accretion flows is one of the promising mechanisms and the so-called “shock oscillation model” has been investigated by many authors (Chakrabarti 1989; Molteni et al. 1999; Chakrabarti et al. 2004; Das et al. 2003a,b; Aoki et al. 2004; Molteni et al. 2006; Okuda et al. 2007). The stability of accretion flows with a standing shock wave in them is one of the key issues.

The linear stability of the standing shock wave against axisymmetric perturbations in the axisymmetric accretion flow is well-known and simply stated as follows: if the post-shock matter is accelerated, the shock is unstable (Nakayama 1994, 1995). However, the accretion shock wave that is stable against axisymmetric perturbations can be unstable for non-axisymmetric perturbations (Molteni et al. 1999; Gu & Foglizzo 2003; Gu & Lu 2005; Nagakura & Yamada 2008). This non-radial shock instability may be quite common. In fact, the similar instability is found in accretion flows onto a nascent proto neutron star in the supernova explosion and might be an important element in the mechanism for it.

Our previous paper (Nagakura & Yamada (2008) hereafter NYv1) investigated general relativistically the non-axisymmetric shock instability around a non-rotating black hole, suggesting also possible implications for fluctuations in GRB jets. However, there is no doubt realistic stellar mass black holes in general are rotating as suggested by the observations of massive stars (Fukuda 1982). Since it is believed that rapidly rotating massive stars are the progenitor of long GRBs, the investigation of the standing accretion shock instability or SASI should be extended to the Kerr black hole. Moreover, in order to take into account the frame dragging due to the black hole’s spin, the fully general relativistic treatment is strongly required. We observed in the previous paper that the general relativistic effects are important to determine the structure of the inner transonic flow. This in turn means that the injection parameters such as Bernoulli constant and specific angular momentum are also affected by the general relativistic effects. In fact, the injection parameters that allow the existence of the standing shock wave are sensitive to the Kerr parameters.

The plan of this paper is as follows. In section 2, we describe the steady axisymmetric accretion flows with a standing shock wave in them. Then we present the formulation of linear analysis in section 3. The numerical methods for dynamical simulations and models are described in section 4. The results of the numerical simulations obtained by both linear analysis and dynamical simulations are shown in section 5. We conclude the paper in section 6 with summary and discussion.

2. Axisymmetric steady accretion flows with a shock wave in Kerr spacetimes

The mathematical formalisms of axisymmetric steady accretion flows onto Kerr black hole with a standing shock wave are essentially the same as those used in NYv1. Only the equatorial plane is considered and the Kerr space metric is fixed in time. The conditions for the existence of multiple sonic points and standing shock waves in Kerr spacetimes were already discussed by (Lu 1986; Lu et al. 1997). In the following we briefly review the essential points for constructing axisymmetric steady flows, which would help the reader to understand the property of the solutions. We refer to Lu (1986); Lu et al. (1997) for more details.

We first determine the range of the injection parameters such as Bernoulli constant and specific angular momentum, these give multiple sonic points. The existence of multiple sonic point is a necessary condition for the existence of standing shock wave, since not only the pre-shock flows but also post-shock flows are transonic. Then, two transonic accretion flows are connected by a standing shock wave, where the Rankine-Hugoniot relations are satisfied. Since the inner transonic flows are strongly affected general relativistic effects, the structure of the entire accretion flows also varies with Kerr parameters.

The basic equations are the relativistic continuity equation and equation of energy-momentum conservations.

$$(\rho_0 u^\mu)_{;\mu} = 0, \quad (1)$$

$$(T^{\mu\nu})_{;\nu} = 0. \quad (2)$$

$\rho_0, u^\mu, T^{\mu\nu}$ are the rest mass density, 4-velocity and energy momentum tensor, respectively. Throughout this paper, we assume a Γ -law EOS, $p = (\Gamma - 1) \rho_0 \epsilon$, where p and ϵ are the pressure, and specific internal energy. Except for the discussion of dynamical simulations, we adopt the geometrical units $G = c = 1$, where G and c are the gravitational constant and the speed of light. Latin and Greek indices denote spatial and spacetime components, respectively. Since we consider the accretion flows only in the equatorial plane, we ignore the θ -component of velocity, u^θ , and all θ derivatives. The basic equations can be reduced to ordinary differential equations with respect to the radial coordinate:

$$\partial_r (r^2 \rho_0 u^r) = 0, \quad (3)$$

$$\partial_r p + \rho_0 u^r \partial_r (h u_r) = \frac{1}{2} \rho_0 h \left\{ (\partial_r g_{rr}) (u^r)^2 + (\partial_r g_{\phi\phi}) (u^\phi)^2 + (\partial_r g_{tt}) (u^t)^2 + 2 (\partial_r g_{t\phi}) u^t u^\phi \right\}, \quad (4)$$

$$\partial_r (h u_t) = 0, \quad (5)$$

$$\partial_r (h u_\phi) = 0, \quad (6)$$

where we use the Boyer-Lindquist coordinates. Here, $g_{\mu\nu}$, h and p are the metric, specific enthalpy and pressure, respectively. The only difference from the equations for the Schwarzschild black hole is the last term in eq. (4), $\{2(\partial_r g_{t\phi})u^t u^\phi\}$, which represents the frame dragging effect. It should be noted, however, that the frame dragging effect is included not only in this term but also in the 4-velocity itself. The transonic flow can be obtained by imposing the regularity conditions at the sonic point (see Lu (1986)), where the equations become apparently singular. Figure 1 shows the locations of the sonic points as a function of the specific angular momentum and Kerr parameter. The adiabatic index and Bernoulli constant are fixed as $4/3$ and 1.004 , respectively in this figure. As is clearly demonstrated, the curve is symmetric with respect to $\lambda = 0$, which λ denotes the specific angular momentum, for the Schwarzschild spacetimes, where as it is not true of the Kerr spacetimes. This is due to the frame dragging of Kerr black holes, which acts effectively as an additional angular momentum that forces a corotation of matter with the black hole, and thus the symmetry is broken. This figure also shows that there are indeed multiple sonic points for adequate injection parameters. It is well known that the physically-meaningful sonic points are the inner and outermost ones, which are so-called saddle-type singularities, while the unphysical middle sonic point is a central-type singularity. Hence, the steady accretion flows with a standing shock wave should pass through the inner- and outermost sonic points. The Rankine-Hugoniot relation determines the location of standing shock wave from these two transonic flows. These equations are completely the same as those used in the previous paper (see Section 2.2 in NYv1). Just like sonic points, the shock positions also vary with the Kerr parameter very much.

As in the Schwarzschild black holes, there are generally two possible shock locations under adequate injection parameters. These are referred to as the inner and outer shock points. We consider only the outer shock in this paper, since it is well known that the inner shock is already unstable against axisymmetric perturbations, which is also true of the Kerr spacetimes (Nakayama 1995). We construct axisymmetric steady accretion flows imbedding on outer shock wave for different injection and Kerr parameters, which are summarized in Table 1. The adiabatic index is fixed to $\Gamma = 4/3$ throughout the paper. It should be noted that some models have negative specific angular momentum, i.e, matter rotates in the opposite direction of the black hole spin, although it is rather unlikely in realistic astrophysical systems. It is, however, useful to elucidate the Kerr parameter dependence and the following fact, which will be demonstrated shortly, also gives another merit: as the Kerr parameter gets larger, the range of the injection parameters that allows the existence of a standing shock wave become smaller and disappears eventually in the corotation case, whereas it is not true for the counter rotation case. This allows us to investigate the properties of the instability under wider injection parameters.

In Figure 2, we show the ranges of injection parameters, for which the standing shock wave can exist. As seen in the left panel, where the corotation case is presented, as the Kerr parameter becomes larger, the allowed regime of the specific angular momentum shifts to smaller values. This is due to the frame-dragging by the Kerr black hole, which acts effectively to increase the angular momentum of matter. Note that the specific angular momentum is conserved along the stream line and frame-dragging effect is not restricted to the vicinity of black hole. The boundary of the allowed regions normally consists of two areas. For a given Bernoulli constant, the maximum angular momentum is determined by the weak shock limit, i.e, Mach number of the shock $M_{sh} \sim 1$. On the other hand, the minimum value is determined by the location of the outer shock wave. It is widely known that the outer shock wave is located at a larger radius than the middle sonic point, while the inner shock wave is located at a smaller radius. If the specific angular momentum becomes smaller, the locations of each shock wave approach the middle sonic point, and eventually coincide at this point. This determines the minimum specific angular momentum for the existence of a standing shock wave. As mentioned in NYv1, however, for small Bernoulli constants, there is a maximum specific angular momentum above which no multiple sonic points exist. This is true only the fully general relativistic treatment. Hence, there is a possibility that the maximum specific angular momentum is determined by this limit. As a matter of fact, there is indeed the case of $a/M_* = 0.9$, in which the allowed regime is bounded by a vertical line for small Bernoulli constants.

The right Figure 2 shows the region of injection parameters, for which the steady shock wave exists in the counter-rotation case, where matter rotates in the opposite direction of the Kerr black hole spin. As expected, the allowed regions are quite different from those for the corotation case. As the Kerr parameter becomes large, the specific angular momentum gets more negative and the Bernoulli constant becomes smaller. Because the frame dragging effects decelerate the matter rotation, the specific angular momentum has to be more negative. As mentioned above, the specific angular momentum is conserved along the stream line, it has too large an absolute value (and hence too great centrifugal force) at distant places from the black hole, where the frame dragging is negligible. The excess should be compensated for by reducing the Bernoulli constant and as a result, pressure.

3. Linearized equations in Kerr spacetimes

We perform a linear analysis for the non-axisymmetric shock instability around a Kerr black hole. The obtained eigen-values help us to analyze not only the shock stability, but also validate the accuracy of dynamical simulations. By combining dynamical simulations with

linear analysis, both the linear and non-linear phases can be investigated in detail. In this section, we present a formulation for the linear analysis including the boundary conditions.

The basic equations are the linearized relativistic continuity and energy-momentum conservation equations. The perturbed quantities are assumed to be proportional to $e^{-i\omega t + im\phi}$. Since we consider the equatorial plane only and neglect all the θ -derivatives and the θ -component of velocity, the linearized equations are expressed as follows:

$$\partial_r f = \frac{i}{\rho_{0(0)} u^{r(0)}} \left\{ \rho_{0(1)} u^{t(0)} \sigma + \rho_{0(0)} (\omega u^{t(1)} - m u^{\phi(1)}) \right\}, \quad (7)$$

$$\partial_r q = \frac{i}{\rho_{0(0)} u^{r(0)} h_{(0)} u^{t(0)}} (\omega p_{(1)} + \rho_{0(0)} u^{t(0)} h_{(0)} u_{t(0)} \sigma q), \quad (8)$$

$$\partial_r V_{(1)} = i \frac{u^{t(0)}}{u^{r(0)}} \sigma V_{(1)}, \quad (9)$$

$$\partial_r S_{(1)} = i \frac{u^{t(0)}}{u^{r(0)}} \sigma S_{(1)}, \quad (10)$$

where S is the entropy per baryon and the following notations are used:

$$f \equiv \frac{\rho_{0(1)}}{\rho_{0(0)}} + \frac{u^{r(1)}}{u^{r(0)}}, \quad (11)$$

$$q \equiv \frac{h_{(1)}}{h_{(0)}} + \frac{u_{t(1)}}{u_{t(0)}}, \quad (12)$$

$$V_{(1)} \equiv \omega (h_{(1)} u_{\phi(0)} + h_{(0)} u_{\phi(1)}) + m (h_{(1)} u_{t(0)} + h_{(0)} u_{t(1)}), \quad (13)$$

$$\sigma \equiv \omega - m \frac{u^{\phi(0)}}{u^{t(0)}}. \quad (14)$$

f and q are the values which relate to the mass flux and Bernoulli constant, respectively. V_1 is a useful value which we can integrate analytically. The σ denotes the complex frequency of the perturbations measured in the rotating frame. Note that these equations for the Kerr spacetimes look completely the same as those used in NYv1 for the Schwarzschild spacetimes. As mentioned in the previous section, however, the frame-dragging effects are included implicitly in the components of 4-velocity. As in the Schwarzschild black hole case, $V_{(1)}$ and $S_{(1)}$ can be integrated analytically (see Section 3 in NYv1), and we only need to integrate numerically Eqs.(7) and (8).

The boundary conditions are also the same as those used in NYv1. We impose the outer boundary condition on the linearized Rankine-Hugoniot relation at the shock surface, assuming that the pre-shock region remains unperturbed. The explicit forms of these equations are given by,

$$(\rho_{0(0)} u^{r(1)})_+ + (\rho_{0(1)} u^{r(0)})_+ + A = 0, \quad (15)$$

$$\left\{ (\rho_0 h u_t u^r)^{(0)} \left(\frac{\rho_{0(1)}}{\rho_{0(0)}} + \frac{h_{(1)}}{h_{(0)}} + \frac{u_{t(1)}}{u_{t(0)}} + \frac{u^{r(1)}}{u^{r(0)}} \right) \right\}_+ + B = 0, \quad (16)$$

$$\left\{ (\rho_0 h u_r u^r)^{(0)} \left(\frac{\rho_{0(1)}}{\rho_{0(0)}} + \frac{h_{(1)}}{h_{(0)}} + \frac{u_{r(1)}}{u_{r(0)}} + \frac{u^{r(1)}}{u^{r(0)}} \right) + p_{(1)} \right\}_+ + C = 0, \quad (17)$$

$$\left\{ (\rho_0 h u_\phi u^r)^{(0)} \left(\frac{\rho_{0(1)}}{\rho_{0(0)}} + \frac{h_{(1)}}{h_{(0)}} + \frac{u_{\phi(1)}}{u_{\phi(0)}} + \frac{u^{r(1)}}{u^{r(0)}} \right) \right\}_+ + D = 0, \quad (18)$$

with the following definitions:

$$A \equiv i\omega\eta \left\{ (\rho_{0(0)} u^{t(0)})_+ - (\rho_{0(0)} u^{t(0)})_- \right\} - im\eta \left\{ (\rho_{0(0)} u^{\phi(0)})_+ - (\rho_{0(0)} u^{\phi(0)})_- \right\}, \quad (19)$$

$$B \equiv i\omega\eta \left\{ (\rho_0 h u_t u^t + p)_+^{(0)} - (\rho_0 h u_t u^t + p)_-^{(0)} \right\} - im\eta \left\{ (\rho_0 h u_t u^\phi)_+^{(0)} - (\rho_0 h u_t u^\phi)_-^{(0)} \right\}, \quad (20)$$

$$C \equiv \left\{ \left(\frac{d}{dr} (\rho_{0(0)} h_{(0)} u_{r(0)} u^{r(0)} + p^{(0)}) \right)_+ - \left(\frac{d}{dr} (\rho_{0(0)} h_{(0)} u_{r(0)} u^{r(0)} + p^{(0)}) \right)_- \right\} \eta + i\omega\eta \left\{ (\rho_0 h u^t u_r)_+^{(0)} - (\rho_0 h u^t u_r)_-^{(0)} \right\} - im\eta \left\{ (\rho_0 h u_r u^\phi)_+^{(0)} - (\rho_0 h u_r u^\phi)_-^{(0)} \right\}, \quad (21)$$

$$D \equiv i\omega\eta \left\{ (\rho_0 h u_\phi u^t)_+^{(0)} - (\rho_0 h u_\phi u^t)_-^{(0)} \right\} - im\eta \left\{ (\rho_0 h u_\phi u^\phi + p)_+^{(0)} - (\rho_0 h u_\phi u^\phi + p)_-^{(0)} \right\}. \quad (22)$$

where η denotes the displacement of the shock radius and defined as:

$$R_{sh} = R_{sh(0)} + \eta \exp(-i\omega t + im\phi), \quad (23)$$

where R_{sh} stands for the shock radius.

Finally, the regularity condition is imposed at the inner sonic point as the inner boundary condition. The explicit form of this condition is;

$$G_{(1)} - F_{(1)} u_{r(0),r} = 0, \quad (24)$$

where the following notations are employed

$$F_{(0)} \equiv \rho_{0(0)} h_{(0)} g^{rr} \left\{ u^{r(0)} u_{r(0)} - (b_{s(0)})^2 (1 + u^{r(0)} u_{r(0)}) \right\} \quad (25)$$

$$F_{(1)} \equiv \rho_{0(1)} h_{(0)} (u^{r(0)})^2 + \rho_{0(0)} h_{(1)} (u^{r(0)})^2 + 2\rho_{0(0)} h_{(0)} u^{r(0)} u^{r(1)} - \Gamma g^{rr} \left\{ p_{(1)} (1 + u^{r(0)} u_{r(0)}) + 2p_{(0)} u^{r(1)} u_{r(0)} \right\}, \quad (26)$$

$$G_{(1)} \equiv \Gamma \left(g^{rr}, r + \frac{2}{r} \right) \left\{ (p_{(1)} u_{r(0)} + p_{(0)} u_{r(1)}) (1 + u_{r(0)} u^{r(0)}) + 2p_{(0)} (u_{r(0)})^2 u^{r(1)} \right\}$$

$$\begin{aligned}
& + \frac{1}{2} \left\{ \rho_{0(1)} h_{(0)} u^{r(0)} + \rho_{0(0)} h_{(1)} u^{r(0)} + \rho_{0(0)} h_{(0)} u^{r(1)} \right\} \\
& \left\{ g_{rr,r} (u^{r(0)})^2 + g_{\phi\phi,r} (u^{\phi(0)})^2 + g_{tt,r} (u^{t(0)})^2 + 2g_{t\phi,r} u^{t(0)} u^{\phi(0)} \right\} \\
& + \rho_{0(0)} h_{(0)} u^{r(0)} \left\{ g_{rr,r} u^{r(0)} u^{r(1)} + g_{\phi\phi,r} u^{\phi(0)} u^{\phi(1)} + g_{tt,r} u^{t(0)} u^{t(1)} + \right. \\
& \left. g_{t\phi,r} (u^{t(0)} u^{\phi(1)} + u^{t(1)} u^{\phi(0)}) \right\} + i\rho_{0(0)} h_{(0)} u^{r(0)} u^{t(0)} u_{r(1)} \sigma \\
& + i\Gamma p_{(0)} (1 + u_{r(0)} u^{r(0)}) (-\omega u^{t(1)} + m u^{\phi(1)}) \\
& - i u^{t(0)} p_{(1)} \sigma.
\end{aligned} \tag{27}$$

The unperturbed sound velocity in the comoving frame and the adiabatic index are denoted by $b_{s(0)}$ and Γ , respectively. Note again that the only explicit modifications from the Schwarzschild spacetime case are the terms with $g_{t\phi}$ (see section 3 in NYv1), although the frame dragging effects are included implicitly in the 4-velocity.

4. Numerical Methods and Models

We perform two dimensional general relativistic hydrodynamical simulations of non-axisymmetric shock instability in the equatorial plane around a Kerr black hole. The numerical methods in the present paper are essentially the same as those used in NYv1.

Our numerical code is based on the so-called central scheme, which guarantees a good accuracy even if flows include shock waves. We refer the reader to the Appendix of NYv1 for more details on this code. The Kerr-Schild coordinates, which have no coordinate singularity and allow us to put the inner boundary inside the event horizon, are used. The computational domain of $0.6r_{eve} \leq r \leq 200M_*$ is covered by the $600(r) \times 60(\phi)$ grid points, where M_* and r_{eve} stand for the black hole mass and the radius of the event horizon in the equatorial plane, respectively. The radial grid width is non-uniform, increasing by 0.34% per zone from the smallest grid ($\Delta r = 0.1M_*$) at the inner boundary. The computational times are $\sim 6 \times 10^4 M_*$, which corresponds to $\sim 500\text{ms}$ for $M_* = 3M_\odot$. In the following, we discuss the numerical results in cgs units for the case $M_* = 3M_\odot$, since we have in mind the application to massive stellar collapses as in NYv1. Note, however, that the formulations are dimensionless, and the scaling is obvious.

The initial perturbation mode has $m = 1$, where m indicates the azimuthal mode number in $e^{im\phi}$, and the amplitude is fixed to 1% (see NYv1 for the dependence on the mode number and the initial amplitude). The radial distributions of initial perturbations are obtained by the linear analysis. We choose the most unstable $m = 1$ mode, which allows us to compare clearly the linear growth phase between the linear analysis and dynamical simulations.

5. Numerical Results

In this section, we first describe the results of the linear analysis, which are obtained by solving Eqs. (7)-(10) with the appropriate boundary conditions at the shock surface and sonic point (see Section 3). Then, we present the time evolutions of shock instability obtained by GRHD simulations in both linear and non-linear phases compared them with the linear analysis. In so doing, we employ the mode decomposition on the shock surface by the Fourier transform:

$$a_m(t) = \int_0^{2\pi} R_{sh}(\phi, t) e^{im\phi} d\phi, \quad (28)$$

where $R_{sh}(\phi, t)$ and $a_m(t)$ are the radius of the shock wave as a function of ϕ and t and the amplitude of mode m as a function of t , respectively.

5.1. Linear Analysis

The real and imaginary parts of unstable eigen-frequencies for the standard Model Mk05E4L301p are given in Figure 3, which also shows the another parts for Model Mk00E4L343p for comparison. In these models, the Bernoulli constant is identical and the Kerr parameter and specific angular momentum are chosen so that the shock radius would become the same. As seen in Figure 3, there are the unstable eigen-frequencies for Model Mk05E4L301p, and we also find that the higher frequency is stable than the lower frequency among these models. It should be noted, however, that this property is not always satisfied (see Fig.5 in NYv1). The magnitude of the imaginary part of omega is slightly larger than the Mk00E4L343p case, because the shock wave for Mk05E4L301p is stronger than Mk00E4L343 case.

Figure 3 also tells us the dependence on the Kerr parameter: the flow tends to be more unstable as the Kerr parameter gets larger. Note that the Bernoulli constant is not changed and the specific angular momentum is chosen in such a way that the shock location is unchanged. This trend is also seen in other models. In Figure 4, we show that the real and imaginary parts of unstable eigen-frequencies for models Mk00E4L350p to Mk0999E4L406i (See Table 1), have the same shock position ($R_{sh} = 35M_*$). As can be clearly seen in this figure, the imaginary part of the eigen-frequency becomes larger in the corotation case, while it becomes smaller in the inverse rotation case (with increasing Kerr parameters). The reason is as follows.

From Table 1, we find that the growth rates and the Mach numbers of the pre-shock flows are correlated with each other. Stronger shocks tend to have a larger imaginary part of eigen-frequency, i.e., they are more unstable. This fact is the key to the above trend. The

inner transonic flow is strongly affected by the frame dragging of the Kerr black hole and it works effectively as an addition to the specific angular momentum of matter. As a result, the specific angular momentum becomes smaller with increasing Kerr parameters if the shock location is fixed. Since the outer transonic flow is hardly affected by the frame dragging effect, this leads to the reduction of the centrifugal force there. As a result, the radial velocity of outer transonic flow becomes faster (slower) in the corotation (counter-rotation) case, and the Mach number of the pre-shock flow gets larger (smaller) with increasing Kerr parameters, which then leads to the trend that the models with larger Kerr parameters tend to be more unstable (stable) in the corotation (counter-rotation) case.

It is also interesting to present the dependence of shock stability on the Kerr parameter under *the same injection parameters*. In Figure 5, we shows the eigen-frequencies for models Mk00E4L345p, Mk005E4L345p and Mk01E4L345p, all corotation cases. The initial steady flows for these models are constructed with the same injection parameters but different Kerr parameters. As found from Table 1, the shock radius becomes larger with increasing Kerr parameters in this case. Recalling our previous results for the Schwarzschild black hole, that the shock radius becomes larger as the specific angular momentum is increased with the same Bernoulli constant, we can interpret the present results as follows: as the Kerr parameter increases, the specific angular momentum becomes effectively larger, and the shock is pushed outwards. Then the Mach number of pre-shock flows becomes smaller, since the radial velocity is a decreasing function of radius. As a result, the flow becomes more stable, or ω_i gets smaller.

In Figures 4 and 5, we find that the unstable eigen-frequencies for higher harmonics oscillate for some models. We think that this is not a numerical artifact, and the oscillatory behavior is found in preceding papers (NYv1, Gu & Foglizzo (2003)). At present, the reason for these oscillations is unclear, and further investigations are necessary.

Finally, we discuss a possible strong correlation between ω_r for the fundamental unstable modes and the shock radius. In Figure 6, we show the shock radii and ω_r for the fundamental unstable modes for all the various models. We also include the previous results (NYv1) in this figure to increase the number of samples. The injection parameters for the previous results are listed in Table 1 in NYv1. As is evident, the real part of fundamental unstable modes decreases monotonically with increasing shock radius even though all models does not have the same injection parameters, adiabatic indices or Kerr parameters. This suggests that the shock radius is the unique factor to decide the oscillation frequency. It also means that the rotational pattern velocity of the deformed shock surface, which corresponds to ω_r , is a function of the shock radii alone. It is interesting that the specific angular momentum has no direct effect on it. The relation will also be useful to infer ω_r from the shock radius without

detailed calculations. At present, we do not understand the reason for this correlation. This may be a clue to the understanding of the mechanism SASI, and definitely needs further investigations.

5.2. Numerical Simulations

Although we investigate several models with different Kerr parameters, the qualitative evolutionary path is generally similar to that found in the previous simulations NYv1. We first summarize the basic features in the temporal evolution of the standard Model Mk05E4L301p, which has the same Bernoulli constant and shock location but a Kerr parameter and specific angular momentum different from Model Mk00E4L343p, which is the standard model M1 in the previous paper (NYv1). Figure 7 shows the snapshots of the velocity for this model. In the linear phase, a purely single $m = 1$ mode grows exponentially and the deformed shock wave starts to form a spiral arm, which rotates in the same direction as the unperturbed flow. Over times, the spiral arm develops and non-linear mode couplings can not be negligible. When the non-linear regime is reached, the dynamics becomes highly complex. Several shocks start to collide with each other and the original shock begins to oscillate radially. While large and small radial oscillations are repeated like a limit cycle, we find that quasi-steady of asymmetric configurations $m = 1$ or 2 are realized eventually for most of the models. For some models that have too large or too small radial oscillations, such as models Mk01E1L350p and Mk02E8L350i, we can not identify the dominant mode in the non-linear phase.

In Table 2, we give the saturation amplitudes of $m = 0$ modes, which vary from model to model. We recognize a strong correlation between the Mach number and the saturation amplitude of axisymmetric $m = 0$ mode: stronger shocks tend to give larger saturation amplitudes. As a matter of fact, the shock wave for Model Mk01E1L350p, which was the largest Mach number, leaves the computational domain soon after the beginning of numerical simulations. On the contrary, the shock wave for Model Mk02E8L350i with the smallest Mach number does not move so much from the initial position throughout the simulation (see Figure 8).

The oscillation timescale and growth rates obtained from the dynamical simulations are in good agreement with those found in the linear analysis (see the left panels of Figures 9 and 10). Thus, we think that the dynamical simulations are accurate enough. As a matter of fact, we have also done the simulations with doubled spatial resolutions both in the r and ϕ directions. The computational domain is covered by $1200(r) \times 120(\phi)$ grid points with the smallest grid of $\Delta r = 0.05M_*$ at the inner boundary. The difference is roughly 10%

at most (see Figure 11).

It is also found from these figures that the results of dynamical simulations start to deviate from those expected by the linear analysis after ~ 6 ms for Model Mk05E4L301p and ~ 30 ms for Model Mk0999E4L406i, which indicates the beginning of the non-linear phase. In fact, in the right panels of these figures, which show the evolution of the axisymmetric $m = 0$ mode, we find that it starts to grow from the time at which the non-linear phase begins. It is important to point out that the duration of the linear phase is much longer in Model Mk0999E4L406i than in Model Mk05E4L301p, since the former is more stable than the latter.

Finally, we compare the obtained growth rates with the acoustic-acoustic and the advective-acoustic cycles between the shock surface and the inner reflection point. This is done to shed light on the instability mechanism. In this analysis, we assume that the inner reflection point is either the corotation radius or the inner sonic point. The procedure in the comparison is completely the same as that used in NYv1 (see Section 5.5 in NYv1). The ratios of the growth rate to the period of each cycle are presented in Figure 12. It is observed that the instability is more likely to be of the Papaloizou-Pringle type. Note, however, that in general the wavelengths of acoustic perturbations are longer than the scale heights (see Table 2) and we can not clearly identify the reflection point, just as in NYv1.

6. Summary and Discussions

This paper is an extension of our previous work NYv1. The non-axisymmetric standing accretion shock instability around a Kerr black hole has been investigated by performing both linear analysis and dynamical simulations with fully general relativistic hydrodynamical treatments. This allows us not only to make clear the dependence of SASI on the Kerr parameter, but also to elucidate the effects specific to the Kerr black hole, such as the frame dragging.

We have explored the range of the injection parameters that allows the existence of a standing shock wave in axisymmetric steady accretion flows and made clear its dependence on the Kerr parameter. In particular, we have demonstrated for large Kerr parameters and small Bernoulli constant in the corotation case, that the maximum specific angular momentum for the existence of standing shock wave is determined by *the limit for the multiple sonic points*. This is qualitatively different from the limit obtained from the pseudo-Newtonian analysis (Gu & Foglizzo 2003).

According to the linear analysis, the shock wave becomes unstable against non-axisymmetric

perturbations, and the frame-dragging effects are also evident. The growth rate of the instability varies widely with the Kerr parameter. Since the inner transonic accretion flow is strongly affected by the frame-dragging from Kerr black hole, the specific angular momentum of matter near the black hole gets effectively increases. If the shock radius is unchanged, the intrinsic specific angular momentum of matter becomes smaller as the Kerr parameter gets larger. As a result, the Mach number of the pre-shock flow becomes larger (smaller) with the increasing Kerr parameter for the corotation (counter-rotation) flow. We have also investigated the dependence of the instability on the Kerr parameter for the same injection parameters instead of the same shock radius in the corotation case. The location of standing shock wave is shifted outward as the Kerr parameter increases, since the inner transonic flow gains effectively the specific angular momentum from the frame-dragging by the black hole, and the centrifugal force is enhanced. We have found that the oscillation frequency of the non-axisymmetric shock wave depends only on the shock radius, irrespective of the injection parameters as well as the Kerr parameters. At the same time, we find a correlation between ω_r for the fundamental unstable mode and the shock radius. The oscillation frequency decreases monotonically with increasing shock radius. Thus, we conclude that the shock radius is the unique factor to decide the oscillation frequency.

In the dynamical simulations, we have observed that the essential evolution of the perturbed system does not change so much from that for the Schwarzschild spacetimes. We have seen that the quasi-steady configuration of $m = 1$ or 2 nature are formed eventually for most of the models, which were also observed in NYv1. The maximum saturation level of average shock radius has been found to be correlated with the Mach number of the pre-shock flow, which is correlated in turn with the eigen-frequency obtained from linear analysis. Hence, the dependence of the saturation level in the non-linear phase on the Kerr parameter can be understood by the result of linear analysis.

It is important to point out that although the ranges of the injection parameters that allows the existence of standing shock wave is not very wide, they are obtained indeed in recent progenitor models (Heger et al. 2005). In fact, if we assume that the black hole mass is $M_* = 3M_\odot$ and the temperature of matter is less than 1 MeV, the range of specific angular momentum for the existence of shock wave is about $\lambda_{cgs} \sim 3 - 5 \times 10^{16}$ cm²/s. Since the standing shock wave is very robust, we believe that a shock wave is formed one way or another provided the injection parameters are appropriate. If such an accretion flow produces GRB somehow, the SASI will be a natural source of fluctuations in the GRB jets.

In order to apply the present results to realistic astrophysical phenomena, such as GRB and QPO, there are many improvements remaining to be made. The radiation, viscosity and magnetic field should be investigated in addition to making the model more self-consistent,

all of which are currently under way. Moreover, needless to say, the structure in the meridian section should be taken into account, which has been a major challenge for many years, since the accretion flow on to the black hole is inevitably transonic and it is difficult to impose a regularity condition at the sonic surface. In this respect, it is encouraging that the problem was solved by the linear perturbation method (Beskin 2002). It should be noted, however, the unperturbed flow is assumed to be spherically symmetric and the specific angular momentum and the frame-dragging by the Kerr black hole are small in the paper. We will need to obtain steady solutions for wider injection and Kerr parameters, which is our future work.

This work was partially supported by the Grant-in-Aid for the 21st century COE program "Holistic Research and Education Center for Physics of Self-organizing Systems" of Waseda University and for Scientific Research of the Ministry of Education, Science, Sports and Culture of Japan (17540267, 14079202).

REFERENCES

- Aoki, S. I., Koide, S., Kudoh, T., Nakayama, K., & Shibata, K. 2004, *ApJ*, 610, 897
- Blandford, R., D., Znajek, R., L., 1977, *MNRAS*, 179 , 433
- Beskin, V., S., 2004, *Les Houches Lect. Notes* **78**, 85
- Chakrabarti, S., K., 1989, *ApJ*, 347, 365
- Chakrabarti, S. K., Acharyya, K. & Molteni, D. 2004, *A&A*, 421, 1
- Das, T. K., Pendharkar, J. K., & Mitra, S. 2003, *ApJ*, 592, 1078 (2003a)
- Das, T. K., Rao, A. R., Vadawale, S. V. 2003, *MNRAS*, 343, 443 (2003b)
- Fukuda, I. 1982, *PASP*, 94, 271
- J. F. Liu, J. N. Bregman, E. Lloyd-Davies, J. Irwin, C. Espaillat and P. Seitzer, *Astrophys. J.* **621**, L17 (2005) [arXiv:astro-ph/0501306].
- Gu, W. M.,& Foglizzo, T. 2003, *A&A*, 409, 1-7
- Gu, W. M.,& Lu, J. F. 2005, *MNRAS*, 365, 647
- Lu, J. F. 1985 *A&A*, 148, 176
- Lu, J. F., Yu, K.N., Yuan, F.,& Young E.C.M 1997, *A&A*, 321, 665

- Heger, A., Woosley, S. E., & Spruit, H.C. 2005, ApJ, 626, 350
- MacFadyen, A., I., & Woosley, S., E., 1999 , APJ 524, 262
- Molteni, D., Toth, G., & Kuznetsov, O. A. 1999, ApJ, 516, 411
- Molteni, D., Gerardi G., Teresi V., 2006, MNRAS, 365, 1405
- Nagakura, H., Yamda, S., (2008) ApJ, accepted.
- Nakayama, K. 1994, MNRAS, 270, 871
- Nakayama, K. 1995, MNRAS, 281, 226
- Okuda, T., Teresi, V., & Molteni, D. 2007, MNRAS, 377, 1431
- Varnié're, P., & Tagger, M. 2002, A&A, 394, 329
- Tagger, M., & Varniere, P. 2006, ApJ, 652, 1457
- Dong, Lai, & David, Tsang 2008, [arXiv:astro-ph/0810.0203v1].

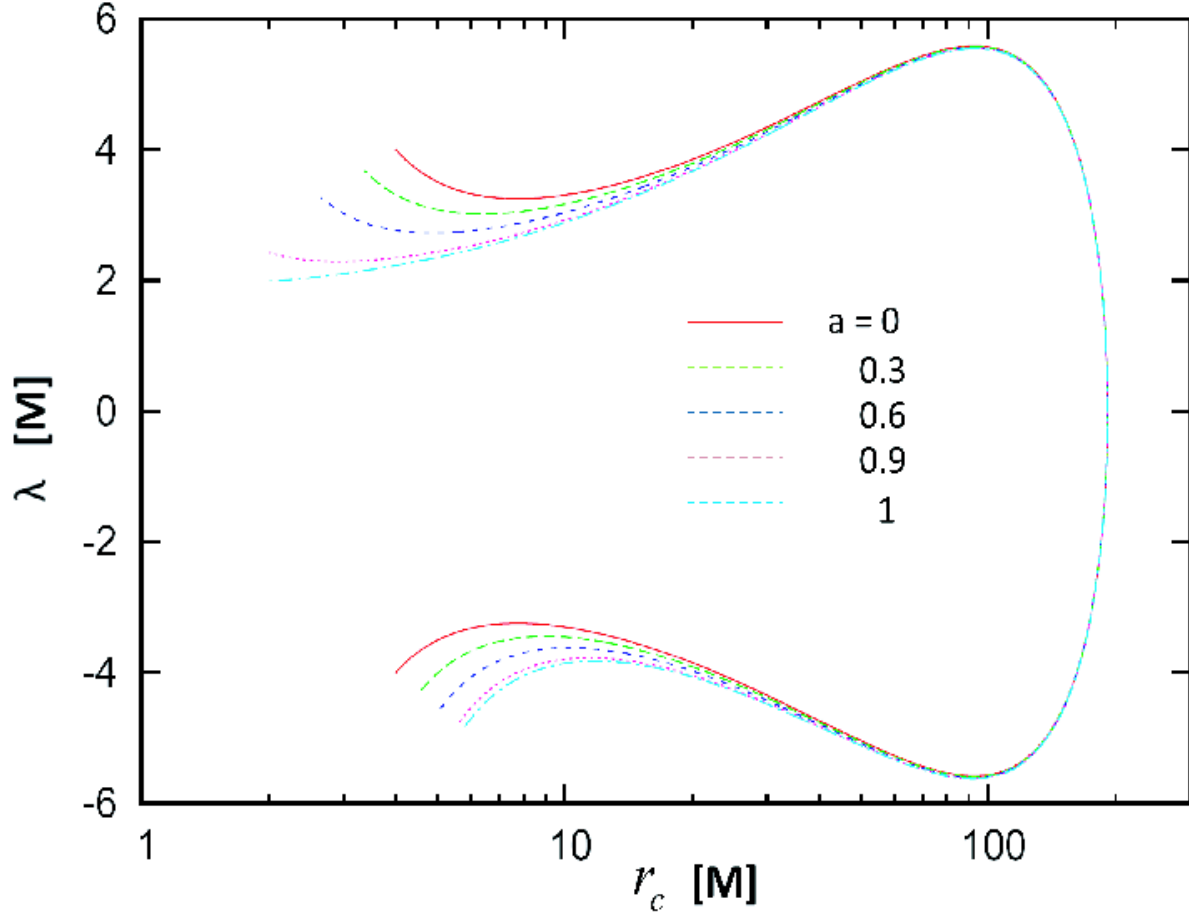


Fig. 1.— The locations of sonic points as a function of the specific angular momentum and Kerr parameter. The adiabatic index and Bernoulli constant are fixed as $3/4$ and 1.004 , respectively.

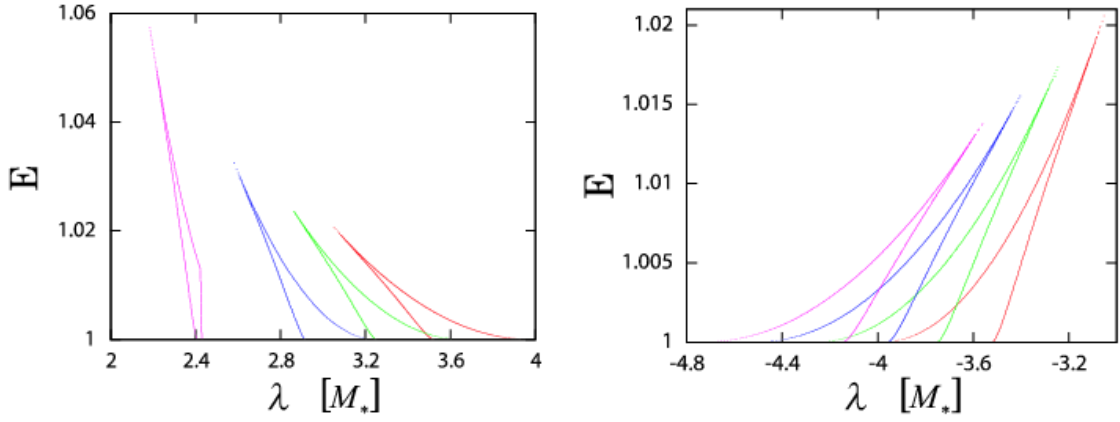


Fig. 2.— The ranges of the injection parameters that allow the existence of a standing accretion shock wave around Kerr black holes. The red, green, blue and pink lines show the boundaries of the allowed regions for $a/M_* = 0, 0.3, 0.6$ and 0.9 , respectively. The left panel shows the corotation case and the right panel gives the counter-rotation case.

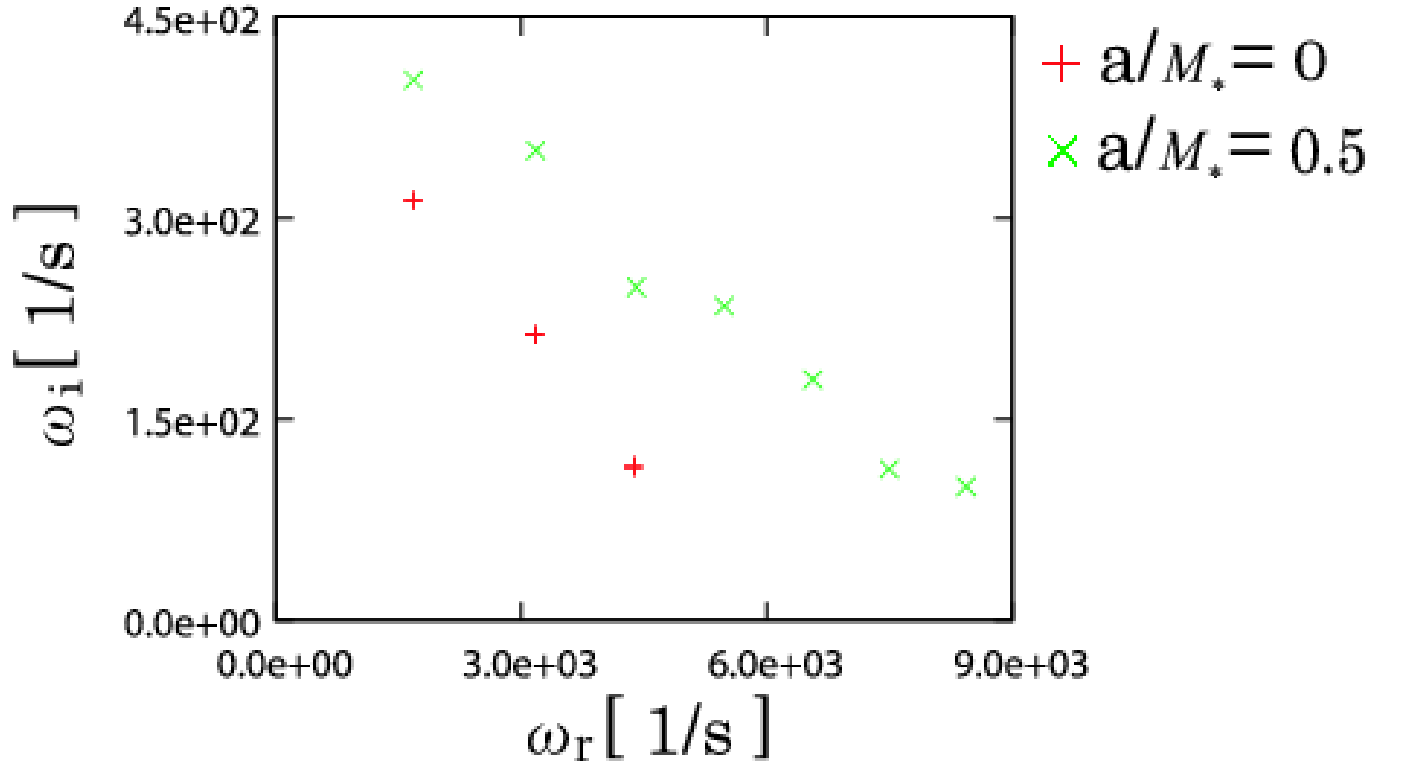


Fig. 3.— The eigen-frequencies of unstable $m = 1$ mode for models Mk05E4L301p (standard model) and Mk00E4L343p. These models have the same shock location ($r = 16M_*$) and Bernoulli constant ($E = 1.004$), but a different Kerr parameter and specific angular momentum.

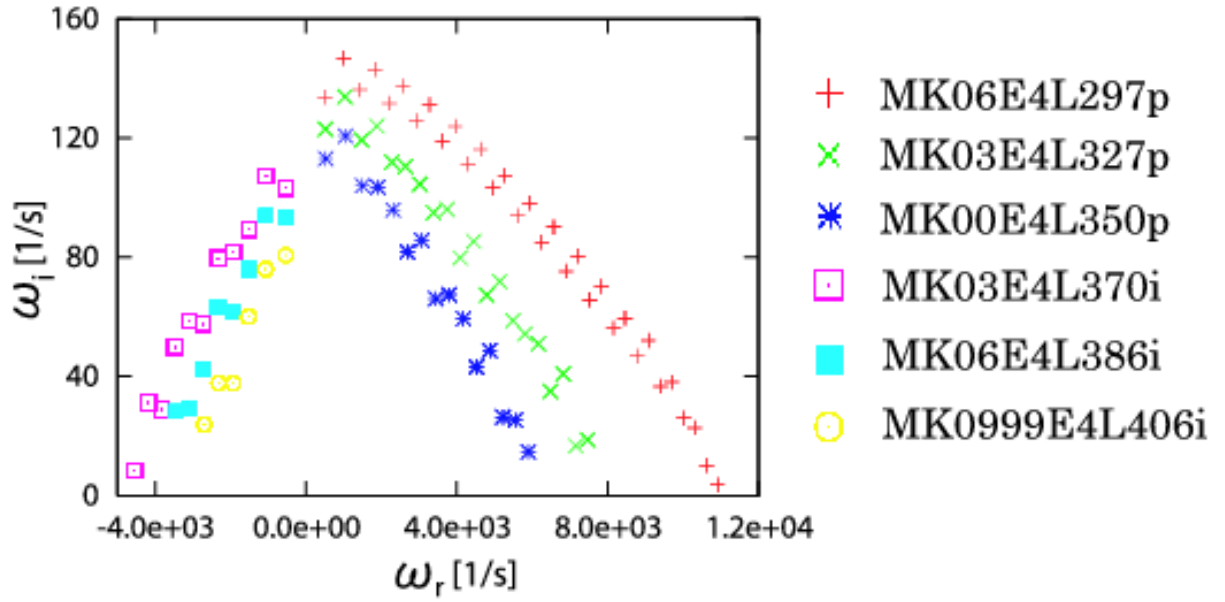


Fig. 4.— The same as Figure 3, but for different models. The shock location of these models is fixed to $r = 35M_*$. Note that the negative values of ω_r correspond to the conter-rotating models.

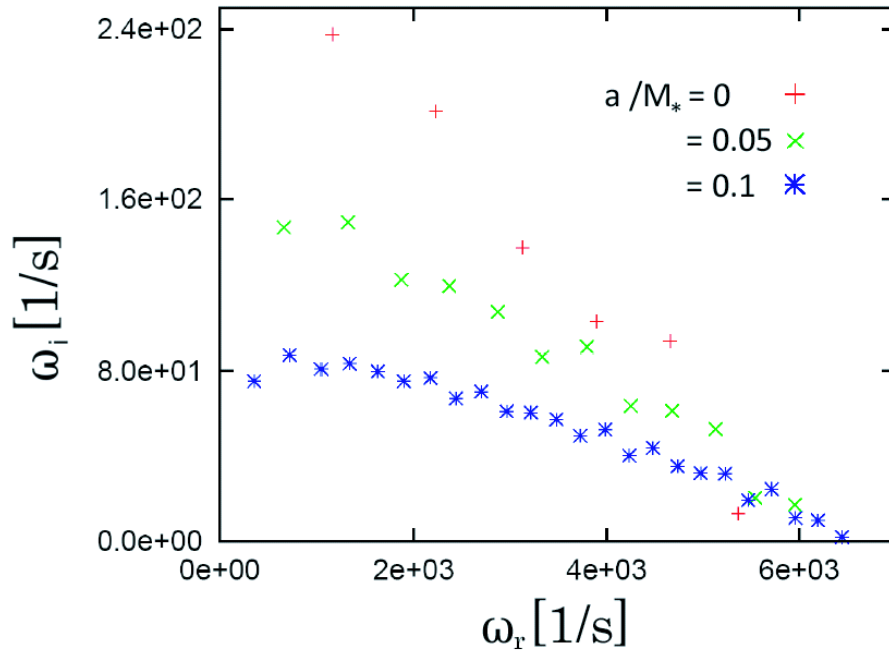


Fig. 5.— The eigen-frequencies of unstable models for the models with the same injection parameters, but different Kerr parameters.

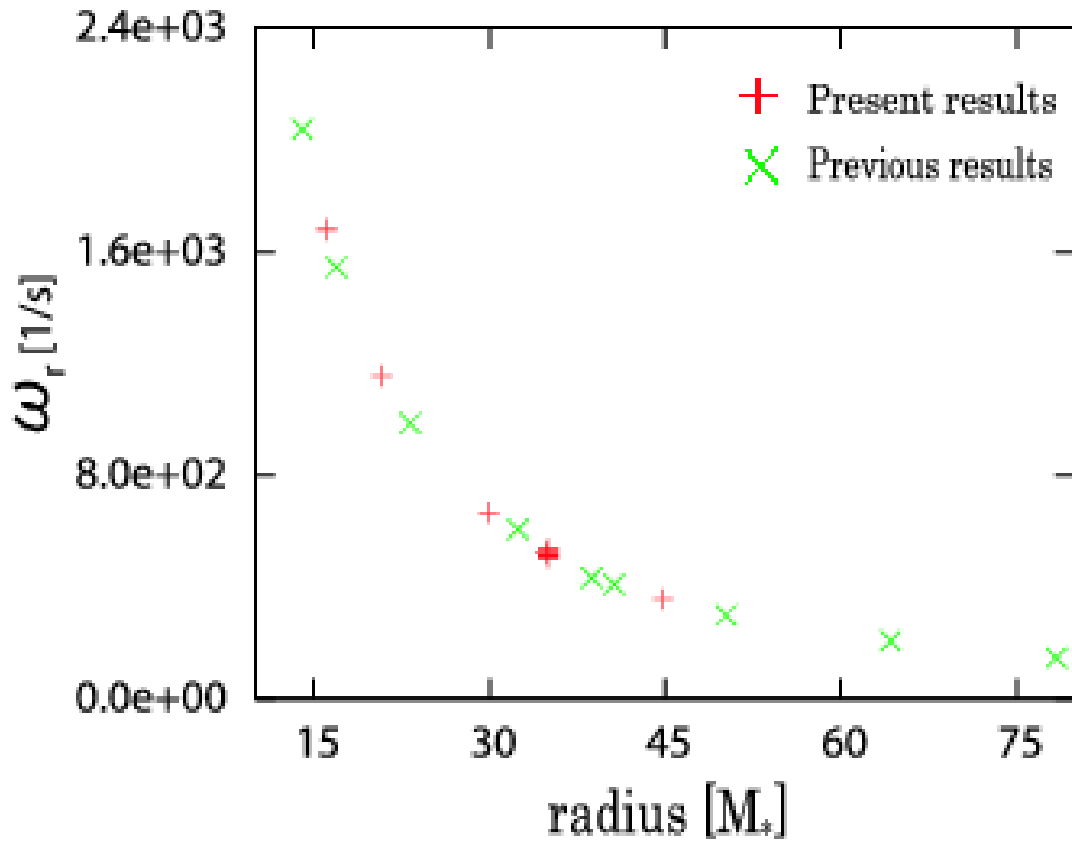


Fig. 6.— The shock radii and the real parts of the eigen-frequencies for the fundamental unstable modes for various models. In addition to the present results (green dots), the previous results (NYv1) are included as red dots.

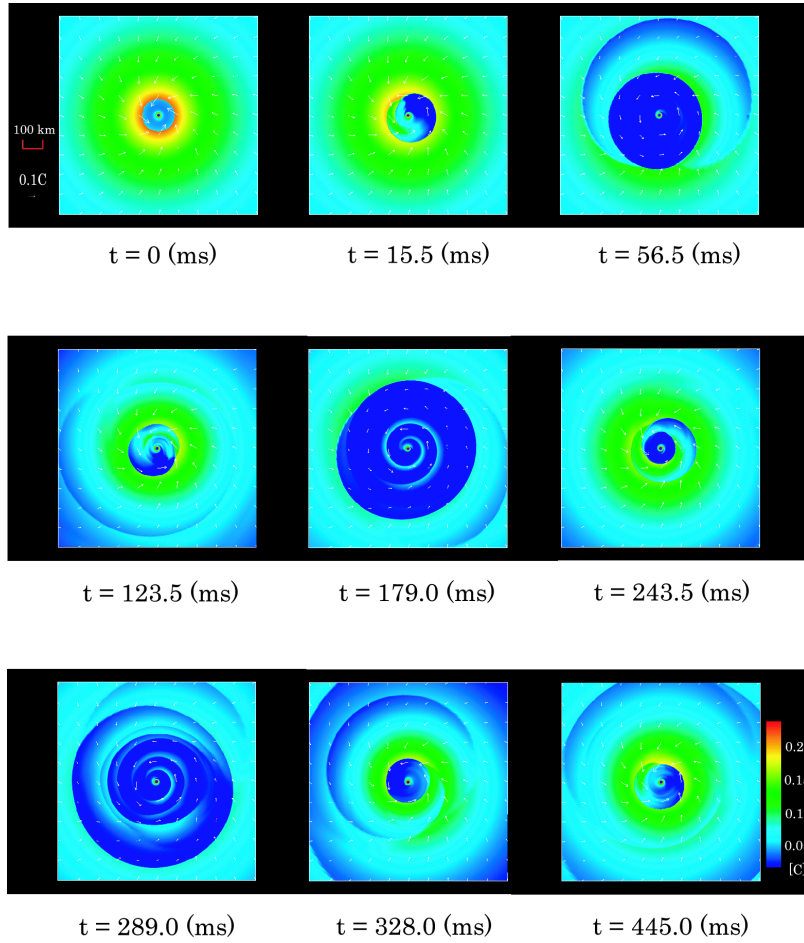


Fig. 7.— The time evolution of the velocity for Model Mk05E4L301p. The color contour shows the magnitude of radial velocity. The arrows represent the velocities at their positions. The central region in blue corresponds to the black hole.

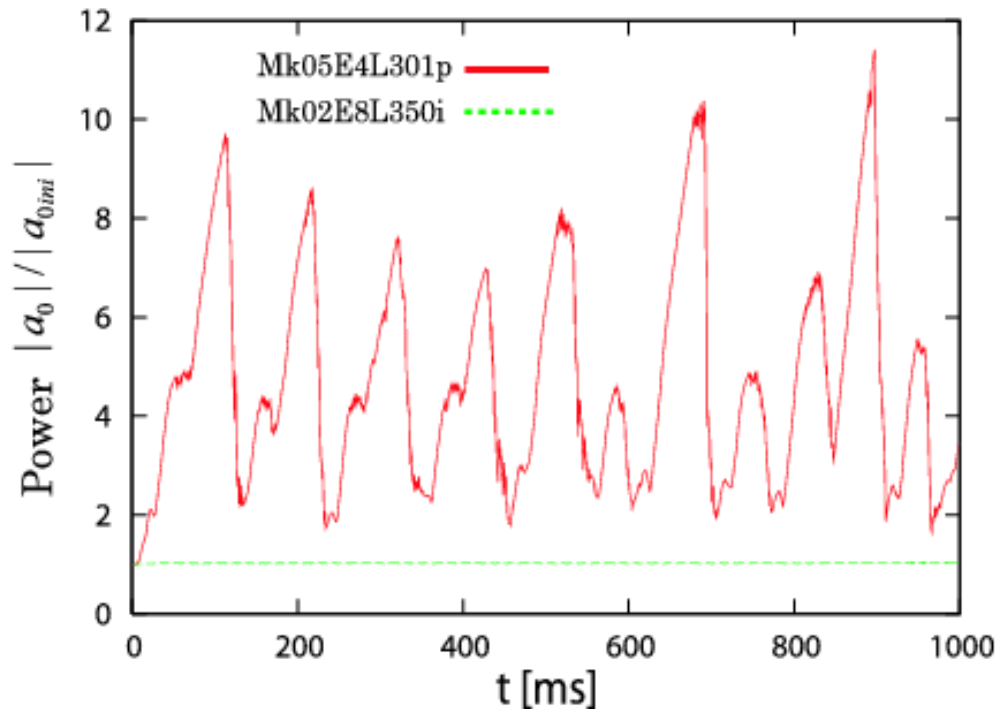


Fig. 8.— The evolutions of the amplitude of $m = 0$ mode for Mk02E8L350i which we evolve long time (1000ms) simulations. The same evolutions for standard Model Mk05E4L301p are also shown for comparison.

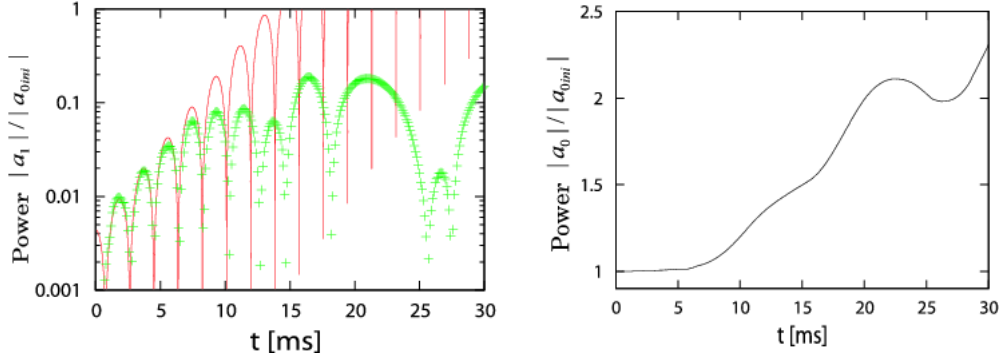


Fig. 9.— The time evolution for Model Mk05E4L301p. Left: the comparison of the time evolutions of the amplitudes of the $m = 1$ mode between the linear analysis (red lines) and dynamical systems (green crosses). Right: the evolutions of the amplitude of the $m = 0$ mode.

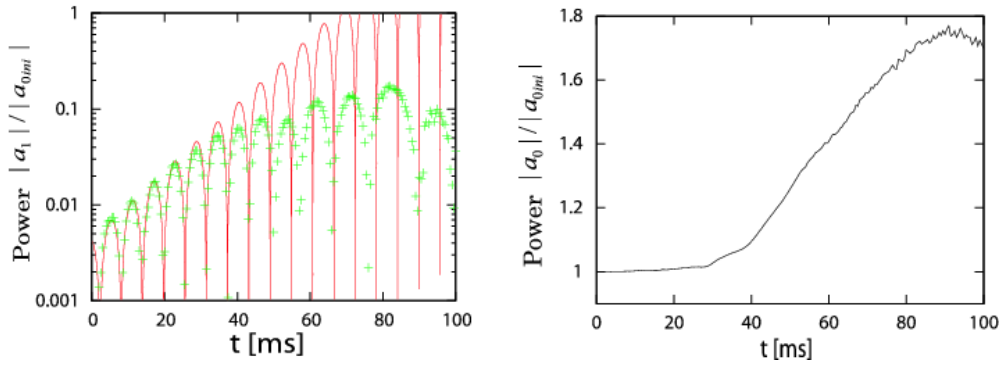


Fig. 10.— The same as Figure 9 but for Model Mk0999E4L406i.

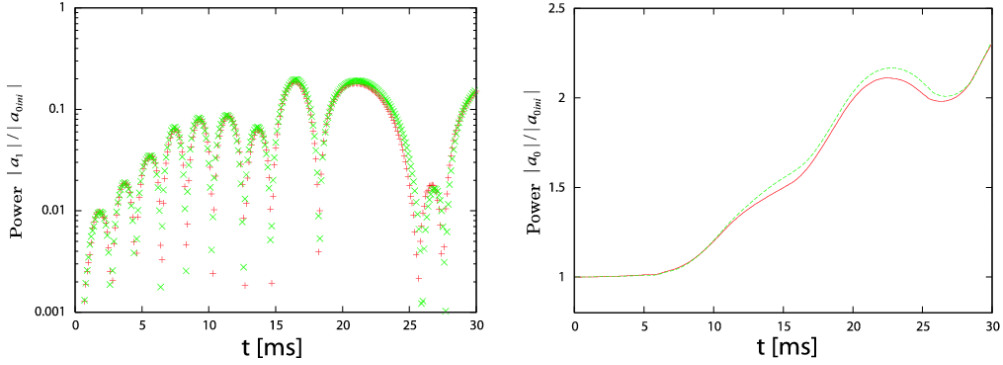


Fig. 11.— The time evolutions of $m = 1$ (left) and $m = 0$ (right) modes for the different resolution for the standard model Mk05E4L301p. The red line is the result for the standard resolution in this paper, the green line is the result for the doubled spatial resolution.

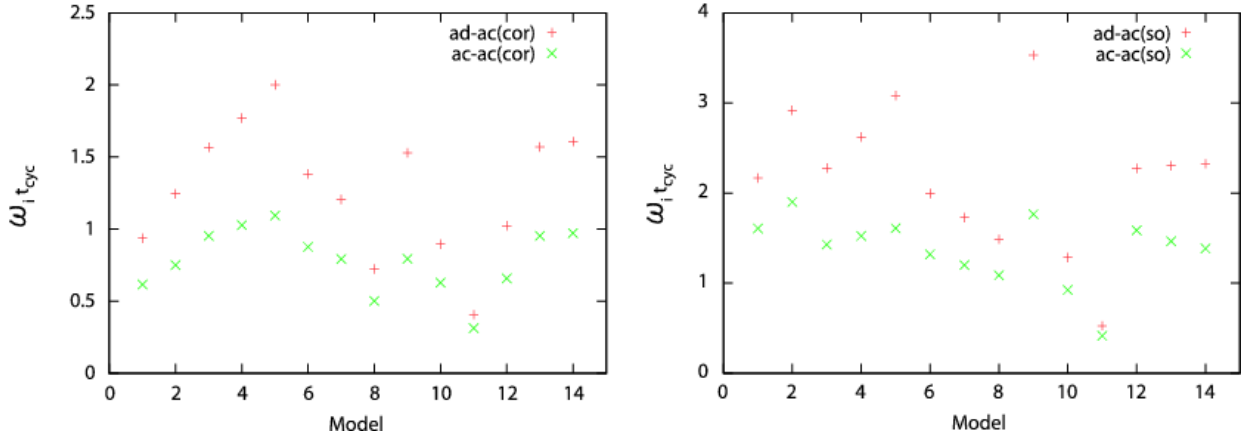


Fig. 12.— The ratio of the growth rate to the frequencies of advective-acoustic (+) and acoustic-acoustic cycle (x) for all the models. In the left (right) panel we assume that the corotation (inner sonic) point is the inner reflection point. See also Figure 10 in NYv1.

Table 1. Model Parameters

Model	Kerr Parameter $a[M_*]$	Bernoulli Constant E	Specific Angular Momentum $\lambda [M_*]$	Inner Sonic Point $r_{inso}[M_*]$	Shock Point $r_{sh}[M_*]$	Mach Number
Mk00E4L343p	0	1.004	3.43	5.3	16.1	2.444
Mk05E4L301p	0.5	1.004	3.01	3.6	16.0	2.682
Mk00E4L350p	0	1.004	3.50	5.0	34.8	2.078
Mk03E4L327p	0.3	1.004	3.27	4.1	35.0	2.137
Mk06E4L297p	0.6	1.004	2.97	3.1	35.0	2.208
Mk03E4L370i	0.3	1.004	-3.70	5.9	35.0	2.019
Mk06E4L386i	0.6	1.004	-3.86	6.8	35.0	1.967
Mk0999E4L406i	0.999	1.004	-4.06	7.9	35.0	1.904
Mk01E1L350p	0.1	1.001	3.50	4.5	35.0	3.426
Mk01E6L350i	0.1	1.006	-3.50	5.6	35.0	1.632
Mk02E8L350i	0.2	1.008	-3.50	6.1	35.0	1.395
Mk00E4L345p	0	1.004	3.45	5.2	20.8	2.355
Mk005E4L345p	0.05	1.004	3.45	4.9	29.9	2.180
Mk01E4L345p	0.1	1.004	3.45	4.6	44.8	1.931

Note. — Parameters for the initial axisymmetric steady flow with a standing shock wave. M_* is the mass of the central black hole.

Table 2. Properties of Instability

Model	maximum amplitude of $m = 0$ mode	Oscillation Period t_{osci}	Growth time $t_{grow}/2\pi$	$ \omega_{r(f)} $ for fundamental node	Wavelength of Acoustic Perturbations λ_w
Mk00E4L343p	3.9	3.7ms	3.2ms	1677	142.6km (31.7 M_*)
Mk05E4L301p	9.7	3.7ms	2.5ms	1681	145.8km (32.9 M_*)
Mk00E4L350p	3.2	5.9ms	8.2ms	525	171.9km (38.2 M_*)
Mk03E4L327p	4.5	6.1ms	7.5ms	517	174.6km (39.4 M_*)
Mk06E4L297p	5.5	6.2ms	6.8ms	503	181.3km (40.9 M_*)
Mk03E4L370i	3.3	5.9ms	9.3ms	531	258.0km (58.2 M_*)
Mk06E4L386i	2.2	5.9ms	10.7ms	535	244.8km (55.3 M_*)
Mk0999E4L406i	1.8	11.7ms	12.4ms	537	458.3km (103.4 M_*)
Mk01E1L350p	5.5	12.5ms	6.0ms	504	343.7km (77.6 M_*)
Mk01E6L350i	1.3	6.0ms	14.1ms	526	279.1km (63.0 M_*)
Mk02E8L350i	1.02	4.3ms	35.7ms	511	202.2km (45.6 M_*)
Mk00E4L345p	4.5	5.4ms	4.2ms	1156	186.5km (42.1 M_*)
Mk005E4L345p	5.6	4.77ms	6.7ms	667	143.9km (32.5 M_*)
Mk01E4L345p	3.8	8.67ms	11.4ms	357	225.2km (50.8 M_*)

Note. — t_{osci} , $t_{grow}/2\pi$ and λ_w represent the oscillation period, growth time and wavelength of acoustic perturbations, respectively, which are obtained by linear analysis. We refer the reader to the NYv1 for the mathematical definitions of these values. $\omega_{r(f)}$ is the real part of unstable fundamental eigen-frequency for each model.